




SAR-based technique for soil permittivity estimation

Yuri Álvarez López ^a, María García Fernández^a, Ana Arboleya Arboleya^a,
Borja González Valdés^b, Yolanda Rodríguez Vaqueiro^b, Fernando Las-Heras^a
and Antonio Pino García^b

5

^aÁrea de Teoría de la Señal y Comunicaciones, Universidad de Oviedo, Gijón, Spain; ^bAtlantTIC Research Center, Universidad de Vigo, Vigo, Spain

ABSTRACT

A conventional synthetic aperture radar (SAR)-based technique for soil permittivity estimation is presented in this contribution. Ground penetrating radar imaging techniques are mainly based on SAR imaging algorithms that take into account the wave velocity in the soil for accurate imaging of buried objects. Reflectometers, datasheets, and indirect observation methods are commonly considered for soil characterization. However, factors such as humidity and temperature may cause some variations in the soil constitutive parameters. This contribution proposes a methodology for *in situ* characterization of soil permittivity, using the known position of a reference object and the application of conventional SAR imaging to recover the reflectivity image, from which the required information to calculate the complex permittivity can be extracted. Experimental validation in both controlled and realistic scenarios proves the capability of the proposed technique to recover the permittivity of different types of soil and to improve the quality of the Underground-SAR image.

ARTICLE HISTORY

Received 10 November 2016
Accepted 15 May 2017

10

15

20

25

1. Introduction

Development of improved imaging techniques for buried objects detection has potential applications in a wide range of different fields, such as civil engineering (identification of pipes and cracks), archaeology (detection of buried ruins), and security applications (landmine detection). In this sense, ground penetrating radar (GPR) is a well-mature technique (Chen et al. 2007; Stove et al. 2013) capable to detect both metallic and dielectric targets (Gamba and Belotti 2003; Daniels 2006).

30

Down-Looking GPR synthetic aperture radar (SAR) systems (Rosen and Ayers 2005) achieve high-resolution in-depth through transmitting ultra-wide-band signals but suffer from strong specular reflections from the ground surface. Most of these systems use transmit and receive antennas mounted at the front or bottom of a moving vehicle and

35

CONTACT Yuri Álvarez López  alvarezuri@uniovi.es  Edificio Polivalente, Módulo 8, Office 1.8.02. Campus Universitario de Gijón. E-33203, Gijón, (Asturias), Spain

Escuela Politécnica de Ingeniería de Gijón, Campus Universitario de Gijón, E33,203, Gijón, Spain. Phone: +34 985,182,541. <http://www.tsc.uniovi.es/investigacion/>

Escuela de Ingeniería de Telecomunicaciones, Campus Universitario, E36310, Vigo, Spain. Phone: +34 986,813,733. <http://atlanttico.uvigo.es/en/>

directed downward. Forward-Looking GPR SAR systems (Liu et al. 2003) use antennas that look ahead of the vehicle, with a standoff distance up to a few tens of metres. These systems achieve worse resolution since they present a smaller effective synthetic aperture but they reduce the reflections from the ground surface and they are safer for the vehicle operator. 40

Multiple SAR-based algorithms as migration techniques (Marpaung and Lu 2014) or Delay-And-Sum (Johansson and Mast 1994), among others, can be used to reconstruct images for buried objects detection. All these methods require the correct soil wave velocity in order to provide a well-focused image and to reduce false alarms. Soil wave velocity is calculated from the knowledge of the soil constitutive parameters, namely conductivity and permittivity. 45

Soil characterization can be done indirectly from datasheets (*Dielectric Constant* 2016), observation methods (Martinez and Byrnes 2001; Wang and Schmutge 1980), measurement of samples in laboratory using waveguide (Gadani and Vyas 2008), coaxial probe techniques (Sreenivas, Venkataratnam, and Rao 1995; Matzler 1998; Komarov, Wang, and Tang 2005; Abdelgwad and Said 2016), and strip-line structures (Vall-Llossera et al. 2005). *In situ* soil characterization can be carried out mainly by means of reflectometers, capable of providing estimation of conductivity, permittivity, and also moisture (Robinson et al. 2003; Skierucha et al. 2012). 50

The use of both a reflectometer and a GPR for accurate subsurface imaging increases the cost and complexity of the system, as in some cases, the cost of a reflectometer is within the same order of magnitude as the GPR. Therefore, the possibility of using the information collected by the GPR to estimate the soil constitutive parameters would avoid the need for a reflectometer, reducing hardware cost. 55

This contribution proposes a simple technique to estimate the complex permittivity of the soil using a simple reference target (e.g. a metallic plate) and the SAR image retrieved from the backscattered field. The method works under the assumption that the soil permittivity is approximately constant in the area to be scanned, which is realistic in some scenarios (e.g. sandy soil scanning). The method can be of interest as a low-cost solution for soil characterization in GPR imaging applications avoiding the need of a reflectometer. 60

The wave velocity can be calculated from the recovered complex permittivity, and it can be employed as input in Underground-SAR imaging algorithm to increase the quality of the reconstructed images. Furthermore, this estimation of the soil losses can be used as well for a priori estimation of the maximum depth at which a target of a given size can be detected. 65 70

2. Methodology

2.1. Underground-SAR imaging

The main purpose of Underground-SAR (Martinez-Lorenzo, Rappaport, and Quivira 2011) is to reconstruct images of underground targets, as opposed to conventional SAR (where the targets are above the ground). Assuming a multiple quasi-monostatic configuration, the transmitting and receiving antennas are in one medium (air), at almost the same location, and the targets are embedded in another medium (e.g. sandy soil). 75

Given a set of scattered field measurements E_{scat} collected on a discrete number of points N and frequencies N_f , the reflectivity at a single point $\rho(\mathbf{r}')$, where \mathbf{r}' is the single point represented as a vector of Cartesian coordinates (x, y, z) , can be calculated as in Equation (1):

$$\rho(\mathbf{r}') = \sum_{n=1}^{N_f} \sum_{m=1}^N E_{\text{scat}}(f_n, \mathbf{r}_m) e^{+j2(\phi_1 + \phi_2)}, \quad (1)$$

where j denotes the imaginary unit, $j = \sqrt{-1}$. ϕ_1 is the phase shift corresponding to a wave propagating from the transmitting antenna (placed at the point \mathbf{r}_m) to the refraction point \mathbf{r}_i at the air–soil interface, and ϕ_2 corresponds to the propagation between \mathbf{r}_i and the underground point (\mathbf{r}') where the reflectivity is computed. f_n denotes each discrete n th frequency. Specifically, these phase shifts are given by Equations (2) and (3), where the wave number in free space for the n th frequency is given by $k_{0,n} = 2\pi f_n / c_0$ (c_0 is the speed of light in the air). $k_{1,n} = k_{0,n} (\epsilon_{r,c})^{1/2}$ is the wave number in a soil with relative complex permittivity $\epsilon_{r,c}$ (where subscripts 'r' and 'c' indicates 'relative' and 'complex'). $\Re(k_{1,n})$ denotes the real part of the wavenumber $k_{1,n}$.

$$\phi_1 = k_{0,n} r_i - r_{m2}. \quad (2)$$

$$\phi_2 = \Re(k_{1,n}) r' - r_{i2}. \quad (3)$$

Therefore, in order to apply this method, the refraction point at the air–soil interface must be estimated. Instead of solving a fourth-order equation (derived from Snell's law), an extension to 3D of the iterative approximation given in Appendix I of Alvarez et al. (2015) is used to estimate \mathbf{r}_i .

If the reconstruction is performed above the ground (i.e. only one medium is considered), then the exponent in Equation (1) equals $+j2k_{0,n} r' - r_{m2}$.

2.2. Material characterization from SAR

If conventional SAR imaging is applied to a background medium with $\epsilon_{r,c} \neq 1$ characterized as free space, it is well known that the echoes of targets in that background medium will appear displaced downwards in the SAR image with respect to their true position due to the slower propagation speed of the waves.

Thus, the composition of the background medium (real part of $\epsilon_{r,c}$) can be estimated provided that the position of a reference target is known. This inverse strategy has been tested in Gonzalez-Valdes et al. (2013) for the characterization of lossless dielectric bodies, but it can also be applied to recover the real part of the permittivity of any medium, provided the reflection associated to the reference target can be identified in the SAR image.

The relationship between the phase terms of Equations (2) and (3) considering air and soil, and the same phase terms but considering air in both cases, for a single frequency and one observation point yields (please refer to the demonstration presented in Gonzalez-Valdes et al. (2013)):

$$2d_{\text{echo}} k_{0,n} = 2d_{\text{obj}} (k_{1,n} - k_{0,n}) = 2d_{\text{obj}} k_{0,n} (\Re(\sqrt{\epsilon_{r,c}}) - 1), \quad (4)$$

where d_{echo} is the distance between the true position of the reference target and the position where the reflectivity associated to that target appears in the SAR image, and d_{obj} is the distance between the air–soil interface and the true position of the reference target. Then, assuming $\Re(\epsilon_{r,c}) \gg \Im(\epsilon_{r,c})$, the real part of the permittivity of the medium can be estimated as in Equation (5):

$$\Re(\epsilon_{r,c}) \approx (1 + d_{\text{echo}}/d_{\text{obj}})^2. \quad (5)$$

The medium losses (imaginary part of $\epsilon_{r,c}$, $\Im(\epsilon_{r,c})$) can also be estimated by taking one additional measurement with the target placed on top of the medium to be characterized. Assuming local plane wave approximation, the reflectivity amplitude difference when the target is buried $|\rho_{\text{buried}}(d_{\text{obj}})|$ and when placed on top of the medium $|\rho_{\text{top}}|$ is given by Equation (6):

$$\ln(|\rho_{\text{buried}}(d_{\text{obj}})|/|\rho_{\text{top}}|) = \alpha d_{\text{obj}}. \quad (6)$$

In Equation (6), α is the attenuation constant in neper (Np) per metre, Np m^{-1} , where neper is the logarithmic unit for ratios of measurements (similar to decibels). The attenuation constant α is related to the imaginary part of the complex wavenumber (and thus the permittivity) as

$$\alpha = k_{0,n} \Im(\sqrt{\epsilon_{r,c}}), \quad \Im(\epsilon_{r,c}) \approx \Im\left(\left(\sqrt{\Re(\epsilon_{r,c})} + j\frac{\alpha c_0}{2\pi f_n}\right)^2\right), \quad (7)$$

where $\Re(\epsilon_{r,c})$ has been estimated previously in Equation (5).

The flow chart of the proposed conventional SAR-based technique for soil characterization is summarized in Figure 1. Note that estimation of $\Re(\epsilon_{r,c})$ just requires one measurement with the reference target buried at known depth, d_{obj} . In the case of $\Im(\epsilon_{r,c})$, an additional measurement with the reference target on top of the medium to be characterized is required.

3. Application examples

In the following sections and subsections, XY , XZ , YZ denote planes. z , y , x denote the position of the XY , XZ , and YZ planes, respectively. X , Y , Z denote size or length.

3.1. XYZ measurement range description

First, the proposed technique has been experimentally validated on a controlled scenario using the XYZ measurement range described in Arboleya, Alvarez, and Las-Heras (2013). A N5244A PNA-X microwave network analyser has been used to collect the measurements. Two helix antennas with S_{11} parameter below -20 dB from 3 to 6 GHz, circular polarization and reverse handedness in a quasi-monostatic configuration, as shown in Figure 2, have been used. The acquisition grid is a rectangular synthetic aperture of size $(X,Y) = (90, 100)$ cm sampled every 2.5 cm, that is, 0.5λ at 6 GHz, and placed 90 cm above the floor of the measurement facility (XY measurement plane at $z = 135$ cm in the coordinate system used in this contribution).

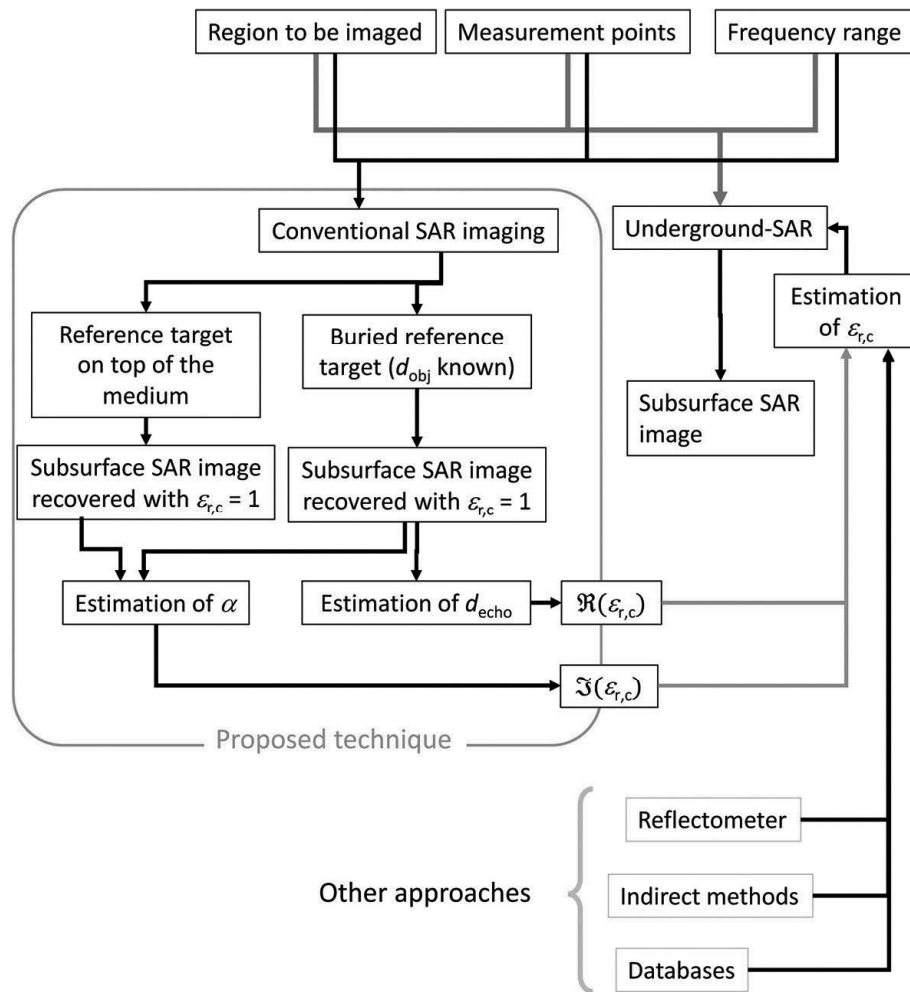
COLOUR
FIGURE

Figure 1. Overview of Underground-SAR imaging and context in which the proposed conventional SAR-based technique for constitutive parameters characterization is introduced.

3.2. Sand characterization

A 10-cm-side square metallic target is employed as reference target for medium characterization. First, two metallic targets are placed on top of a plastic box of size $(X, Y, Z) = (45, 62, 32)$ cm filled with dry sand up to a height of 22 ± 1 cm (see Figure 2). The measurement facility floor has a layer of absorbers on top of a metallic plate, which had to be partially removed to avoid damaging, so the sand box is placed right above the metallic plate.

Conventional SAR imaging is applied to the scattered field measurements to compute the reflectivity of the sand box with the two metallic targets on top. Results are depicted in Figure 3 for XZ (Figure 3(a)) and YZ (Figure 3(b) and 3(c)) planes. Reflectivity is normalized with respect to the maximum of all the SAR images of Section 3.2.

Next, the two metallic targets are buried in the sand at a depth of $d_{obj} = 9$ cm. Again the scattered field is measured and conventional SAR imaging is applied to obtain the reflectivity. Results are depicted in Figure 3(d)–(f) for XZ and XY planes. Placement of the two metallic targets can be clearly noticed (Figure 3(d), XY plane at $z = 50$ cm, and Figure 3(f)). Note the lower reflectivity with respect to the case where the targets were on top of the sand. As expected, these reflections occur deeper than the position where

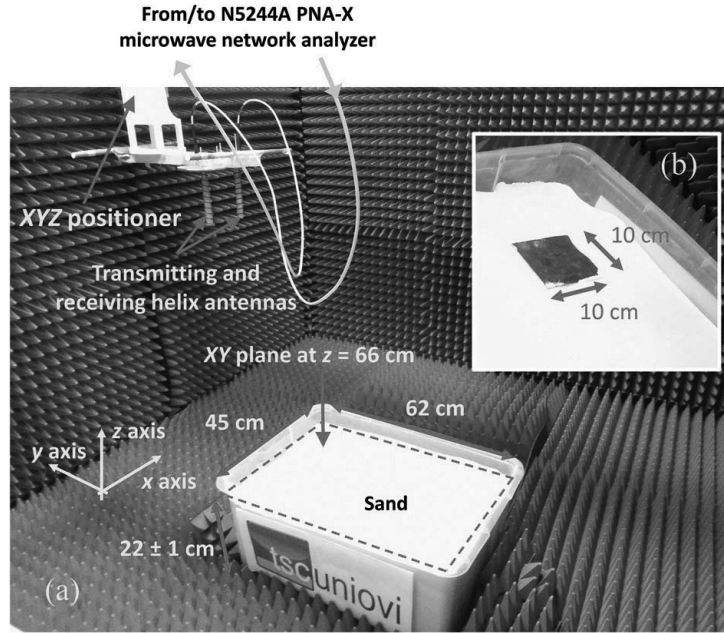
COLOUR
FIGURE

Figure 2. (a) Measurement setup: XYZ positioner, transmitting and receiving antennas, and sand box. (b) Detail of the metallic target used as reference.

the metallic targets actually are (it should be at the XY plane at $z = 57$ cm). Sand complex permittivity can be recovered from the knowledge of d_{obj} , d_{echo} , and the SAR images. From Figure 3(d) and $d_{obj} = 9$ cm, $d_{echo} = 66 \pm 1$ cm $- 9$ cm $- 50$ cm $= 7 \pm 1$ cm. Thus, applying Equation (5), $\Re(\epsilon_{r,c})$ is estimated within the range [2.7 3.5].

175

For $\Im(\epsilon_{r,c})$ the amplitude of the normalized reflectivity associated to the metallic target on top of the sand box, $|\rho_{top}|$, and buried in the sand, $|\rho_{buried}(d_{obj})|$, is considered. From Figure 3 (a) $|\rho_{top}| = -5 \pm 1$ dB ($z = 66$ cm), and from Figure 3(d) $|\rho_{buried}(d_{obj})| = -12 \pm 1$ dB ($z = 50$ cm). After applying Equation (6), $\alpha = [7.7 10.2]$. The imaginary part of the permittivity is calculated from Equation (7) (centre frequency, $f = 4.5$ GHz, is considered), $\Im(\epsilon_{r,c}) = [0.27 0.41]$.

180

The echo of the metallic plate (the measurement facility floor) below the sand box can also be noticed (Figure 3(a) and 3(d), $z = 28$ cm). As the sand thickness is $d_{sand} = 22 \pm 1$ cm, the echo due to the reflection on the metallic plate of the measurement facility floor is $d_{floor,echo} = 66 \pm 1$ cm $- 22$ cm $- 28$ cm $= 16 \pm 1$ cm. From d_{sand} and $d_{floor,echo}$ the real part of the permittivity is estimated yielding $\Re(\epsilon_{r,c}) = [2.8 3.3]$, which is in agreement

185

3.3. Loamy soil characterization

Second test is devoted to analyse a different kind of medium with higher losses than sand. For this purpose, a second box has been filled with 20 ± 1 cm of loamy soil, as shown in Figure 4(a). A larger 20 cm \times 20 cm metallic plate has been chosen as reference target due to the fact that the higher losses of loam prevent the 10 cm \times 10 cm to be detected even if shallowly buried. The sand box is placed next to the loam for reference purposes and also to test the detectability of an arbitrary-shaped metallic target (Figure 4(b)).

190

Conventional SAR imaging has been applied to the following cases: (i) the metallic plate is placed on top of the loamy soil and there is no metallic target in the sand

195

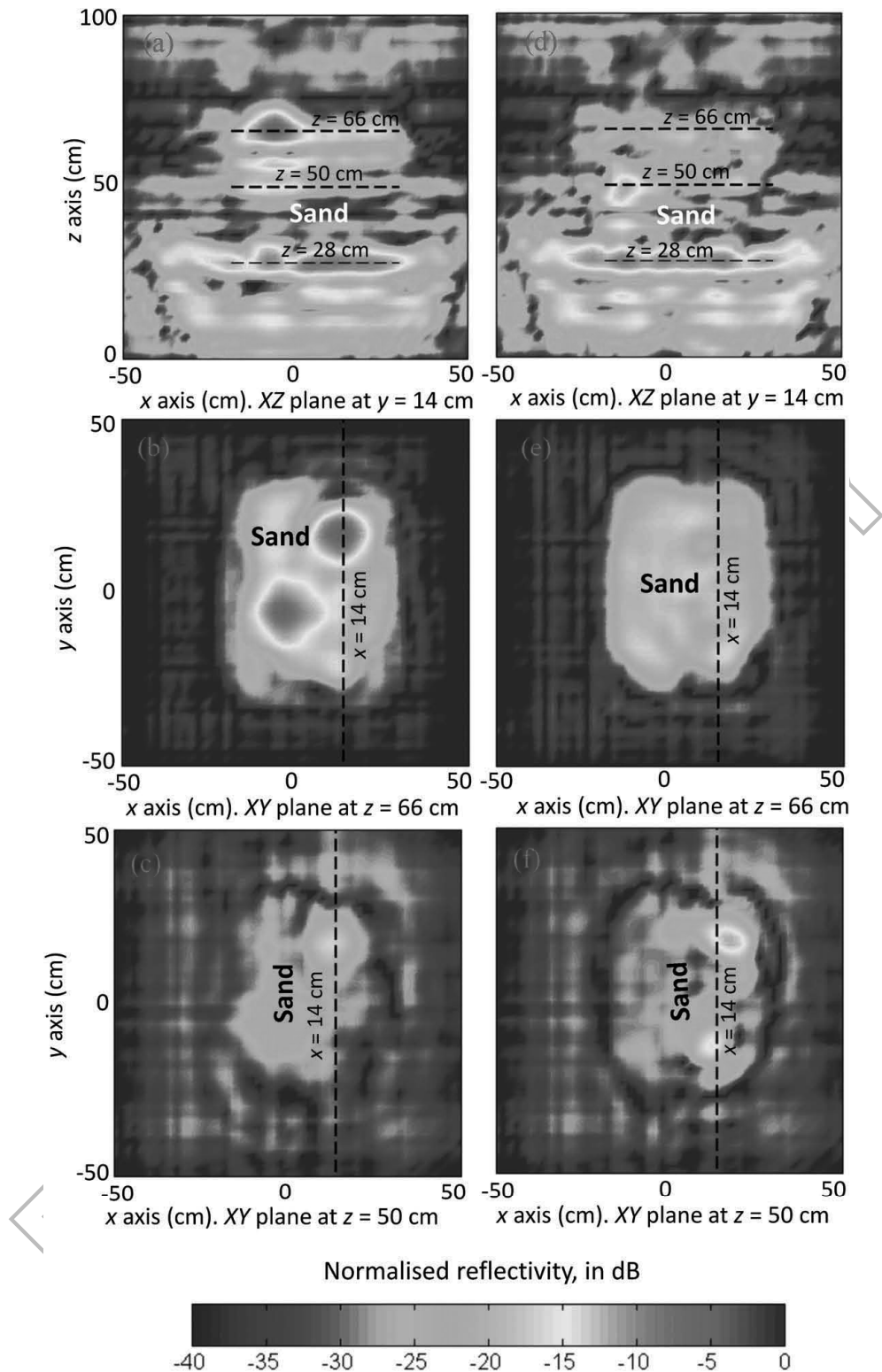


Figure 3. Reflectivity SAR images. Two metallic targets placed on top of a sand box (a–c) and buried in the sand (d–f). (a,d) XZ cut, plane $y = 14$ cm. (b,e) XY cut, plane $z = 66$ cm (sand surface). (c,f) XY cut, plane $z = 50$ cm. Air–sand interface: $z = 66 \pm 1$ cm.

(Figure 5(a) and 5(d)); (ii) the metallic plate is buried $d_{\text{obj,large}} = 4$ cm in the loamy soil, and the arbitrary-shaped metallic target of Figure 4(b) is buried $d_{\text{obj,arb}} = 5$ cm in the sand (Figure 5(b) and 5(e)); and (iii) there are no targets buried neither in the sand nor in the loamy soil (Figure 5(c) and 5(f)).

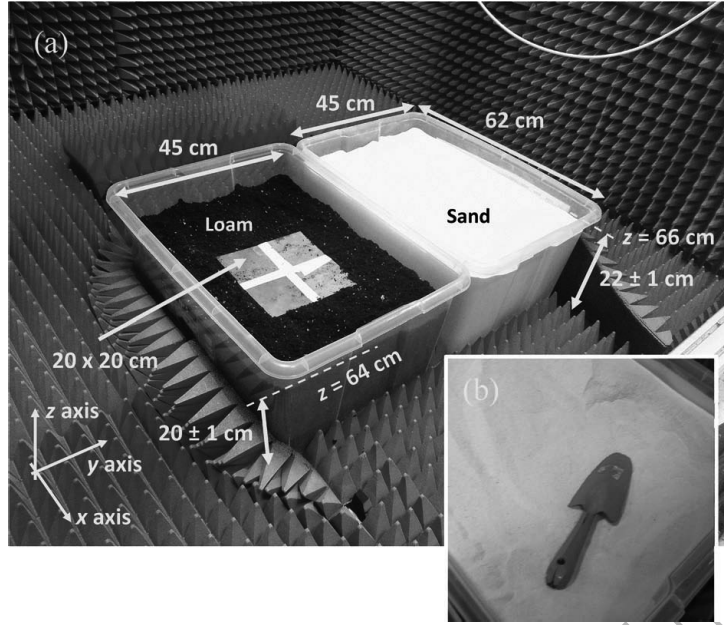
COLOUR
FIGURE

Figure 4. Measurement setup. (a) Two boxes filled with loamy soil and sand. A 20 cm × 20 cm metallic plate is used as reference object for the loamy soil. (b) Metallic object buried in the sand.

A qualitative analysis of the reflectivity for the three cases depicted in Figure 5 shows that: (i) the loam losses are so high that the reflection from the metallic plate below the plastic boxes cannot be detected. Note the high detectability in the case of sand ($z = 28$ cm, Figure 5(a)–(c)); (ii) even being the 20 cm × 20 cm metallic plate larger than the arbitrary shape object, their detectability is similar (Figure 5(b) and 5(e)), in agreement with the expected sand and loam losses.

Next, the complex permittivity of the loam is recovered from the reflectivity values of Figure 5. Given $d_{\text{obj,large}} = 4$ cm and $d_{\text{echo,large}} = 6 \pm 1$ cm, then $\Re(\epsilon_{r,c}) = [2.5 \ 3.2]$. In the case of the imaginary part, $\Im(\epsilon_{r,c})$, $|\rho_{\text{top,large}}| = 0 \pm 1$ dB from Figure 5(a) ($z = 64$ cm) and $|\rho_{\text{buried,large}}(d_{\text{obj,large}})| = -7 \pm 1$ dB from Figure 5(b) and 5(e) ($z = 54$ cm). After applying Equation (6), $\alpha = [17.3 \ 23.0]$. Finally, from Equation (7), the imaginary part of the permittivity is estimated within the range $\Im(\epsilon_{r,c}) = [0.58 \ 0.88]$, that is, twice the one for sandy soil.

3.4. Stratified media

The proposed technique for medium characterization is based on the assumption that the constitutive parameters remain constant within the volume of interest. Its extension to stratified media is tested by means of a simple experiment. The upper part of the loamy soil box has been emptied and filled with 11 ± 1 cm of sand, as shown in Figure 6. In this case, the goal is to check if it is possible to identify the different layers of the soil in the box with two media. For this experiment, no metallic objects have been buried.

After applying conventional SAR imaging, the recovered reflectivity is depicted in Figure 7. For the sand box, the air–sand interface as well as the echo associated to the reflection on the metallic floor of the measurement facility ($d_{\text{floor,echo}}$) is again noticeable (Figure 7(a) and 7(c), $z = 32$ cm) as in the previous experiments. The estimation of the permittivity agrees too, since $d_{\text{sand}} = 18 \pm 1$ cm and $d_{\text{floor,echo}} = 14 \pm 1$ cm, which yields $\Re(\epsilon_{r,c}) = [2.8 \ 3.5]$. In the case of the

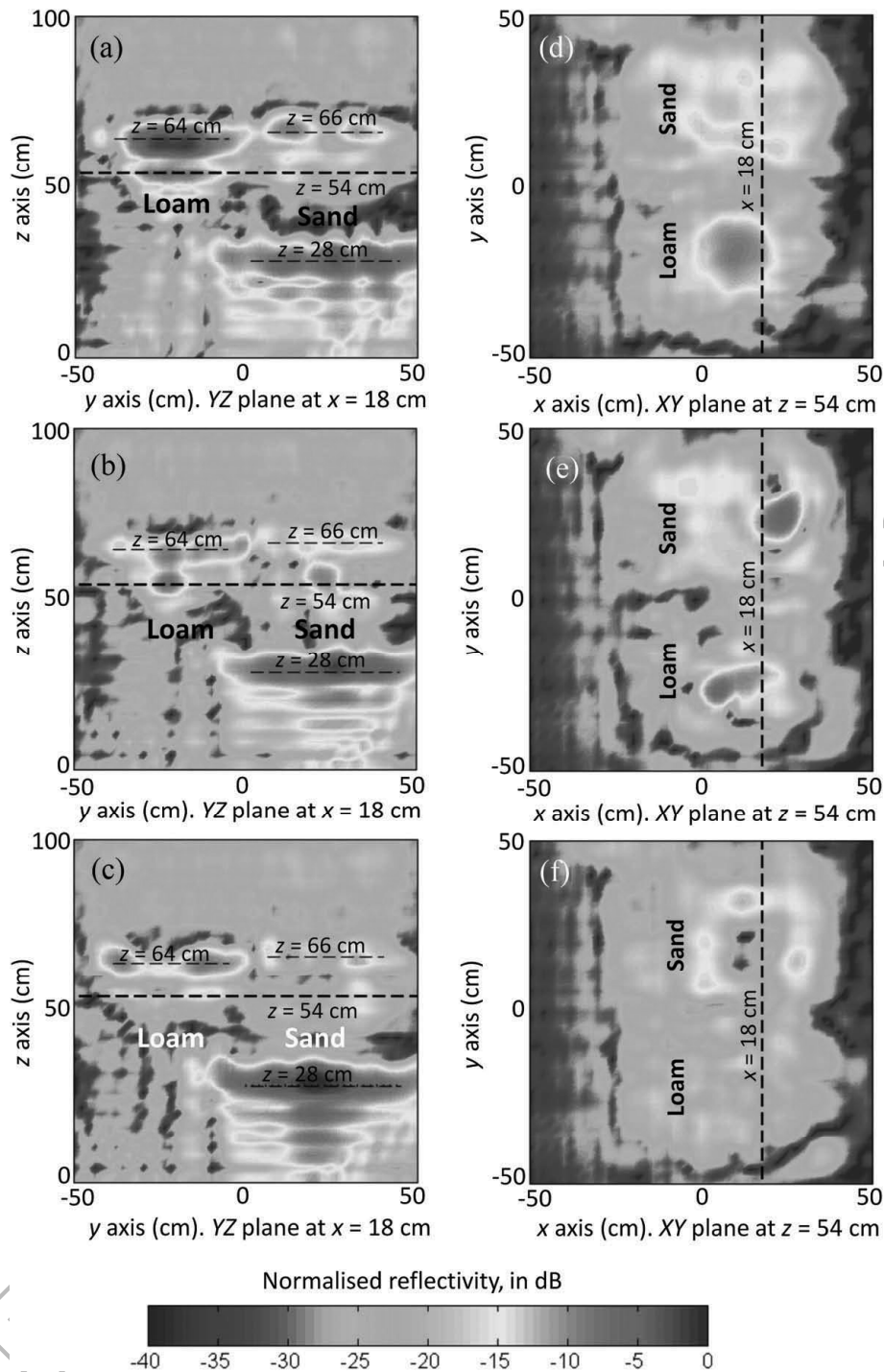
COLOUR
FIGURE

Figure 5. Reflectivity SAR images. A metallic target placed on top of a loamy soil box (a,d), two metallic targets buried in loam and sand respectively (b,e), and sand and loamy soil boxes with no targets on it (c,f). XZ planes: (a–c). XY planes: (d–f). Air–sand interface: $z = 66 \pm 1$ cm. Air–loam interface: $z = 64 \pm 1$ cm.

two media box, Figure 7(b) and 7(c), the air–sand interface is clearly noticeable ($z = 70$ cm), but also the sand–loam interface ($z = 50$ cm). The higher losses of loam prevent from the detection of the echo due to the metallic floor. If the depth of the sand layer is known, $d_{\text{sand}} = 11 \pm 1$ cm, as well as the depth of the echo associated to the reflection on the sand–loam interface, $d_{\text{sand-loam,echo}} = 70 \pm 1$ cm – 11 cm – 50 cm = 9 ± 1 cm, then it is possible to estimate the complex permittivity yielding $\Re(\epsilon_{r,c}) = [2.8 \ 4]$.

225

230

COLOUR
FIGURE

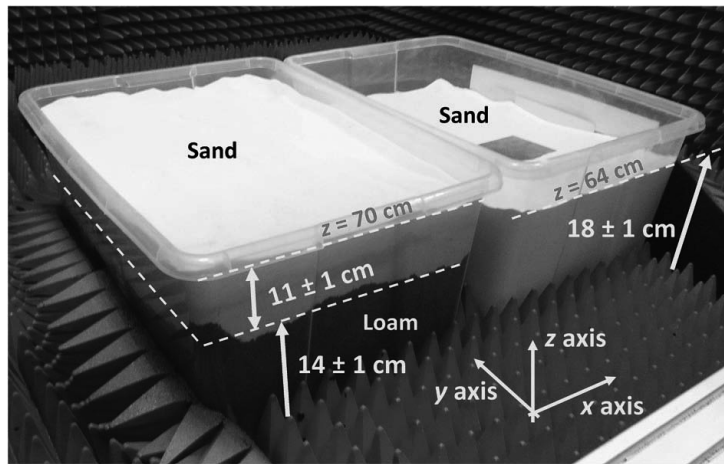


Figure 6. Measurement setup. Left box filled with loamy soil up to a height of 14 ± 1 cm, with a layer of sand on top. Right box filled with sand.

COLOUR
FIGURE

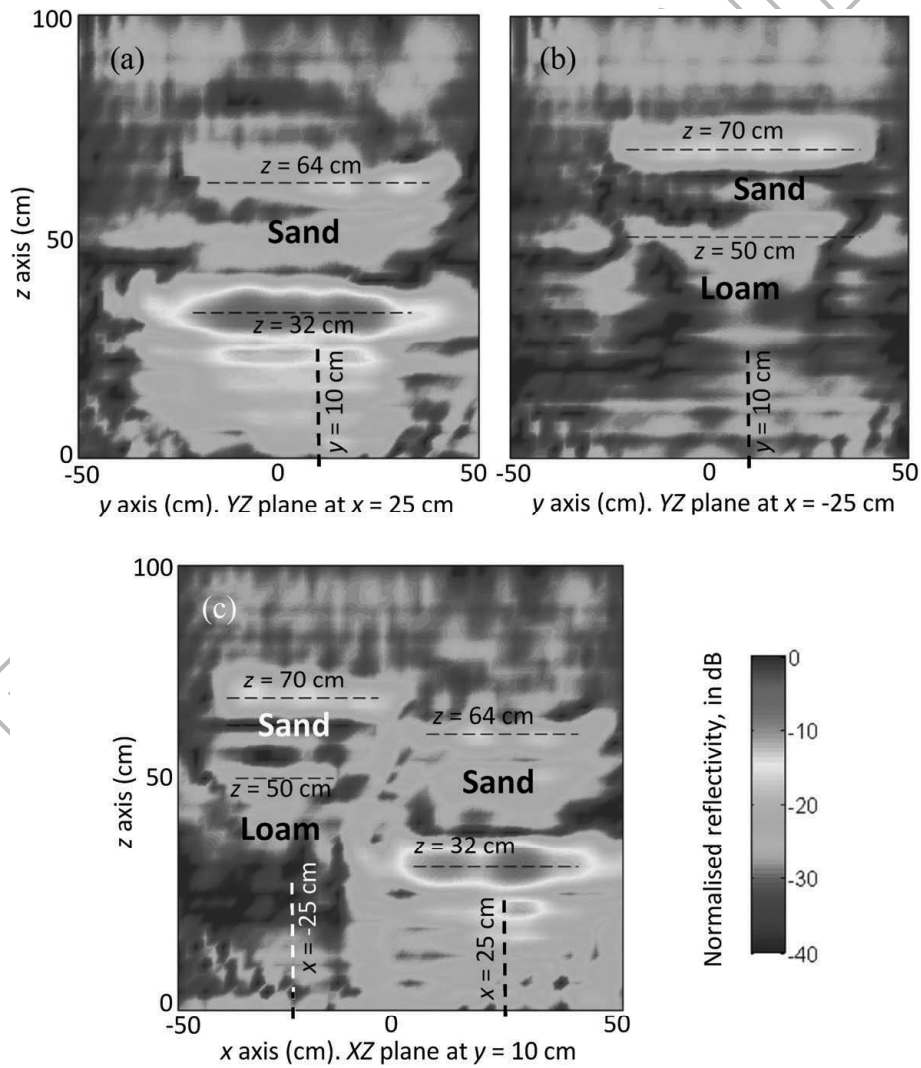


Figure 7. Reflectivity SAR images. YZ cuts: (a) air–sand interface: $z = 64 \pm 1$ cm, (b) air–sand interface: $z = 70 \pm 1$ cm, and sand–loam interface: $z = 50 \pm 1$ cm. (c) XZ cut.

3.5. Mixed soil

To conclude this section, a more complex setup has been considered. The sand box has been replaced by a smaller box containing a 50% mix of sand and loam. Half of the box filled with a layer of sand and a layer of loam has been emptied in order to refill that half with the 50% mix of sand and loam, as shown in Figure 8. Notice the different heights of the different media. 235

A first measurement with no objects buried has been taken. Next, the 10 cm × 10 cm metallic reference target has been buried at a depth of $d_{\text{obj}} = 7$ cm in the box filled with mixed soil. Finally, the reference object has been placed on top of the mixed soil concerning soil losses estimation. 240

Results for the recovered reflectivity using conventional SAR imaging are shown in Figure 9. First, results for the boxes with no metallic objects on them are depicted (Figure 9(a)–(d)). The different air–sand ($z = 70$ cm), air–mixed soil ($z = 58$ cm), and sand–loam interfaces ($z = 50$ cm) can be identified. The losses of the mixed soil are still large enough to allow the detection of the echo associated to the metallic floor of the measurement facility, even in the case of the small box, filled just up to $d_{\text{mix}} = 14 \pm 1$ cm. 245

Figure 9(e) and 9(f) corresponds to the SAR images when the metallic target is buried $d_{\text{obj}} = 7$ cm in the small box. The echo appears at $d_{\text{echo}} = 5 \pm 1$ cm, thus from Equation (5), $\Re(\epsilon_{r,c}) = [2.4 \ 3.4]$. To recover the imaginary part of the permittivity, the metallic target is placed on top of the mix soil (Figure 9(g) and 9(h)), recording the reflectivity amplitude. From Figure 9(e) and 9(f), $|\rho_{\text{buried}}(d_{\text{obj}})| = -13 \pm 1$ dB ($z = 46$ cm), and from Figure 9(g) and 9(h), $|\rho_{\text{top}}(d_{\text{obj}})| = -5 \pm 1$ dB ($z = 58$ cm). Then, $\alpha = [11.5 \ 14.8]$. And finally, after applying Equation (7), $\Im(\epsilon_{r,c}) = [0.38 \ 0.58]$. 250

A summary of the soil characterization results is presented in Table 1, together with the references where typical permittivity values for these kinds of soils can be found. It must be remarked that the experiments were conducted in a dry environment, so the moisture content of the soil is expected to be less than 10%. It can be noticed a good agreement between the values given in the literature using reflectometry, measurement 255

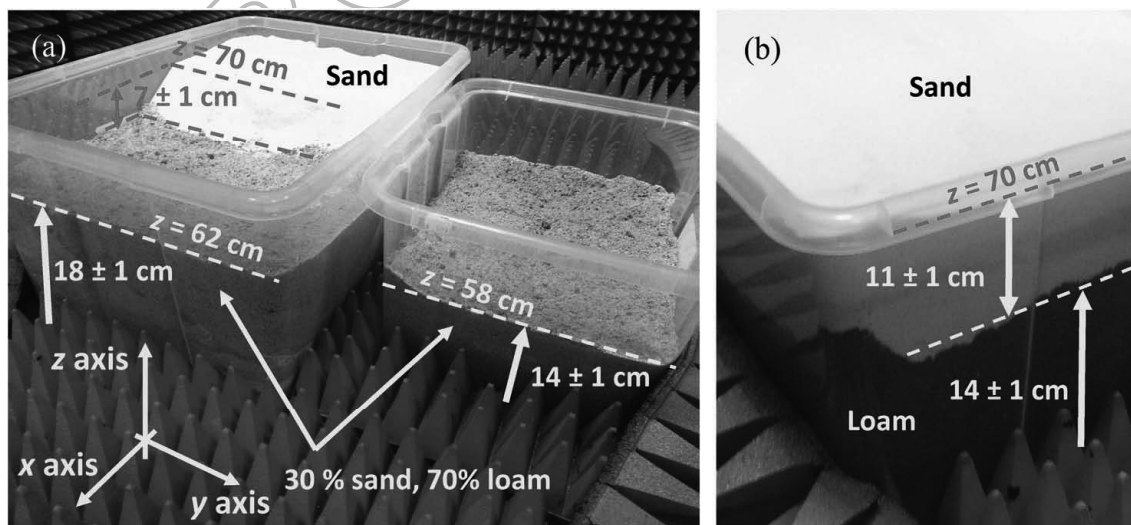
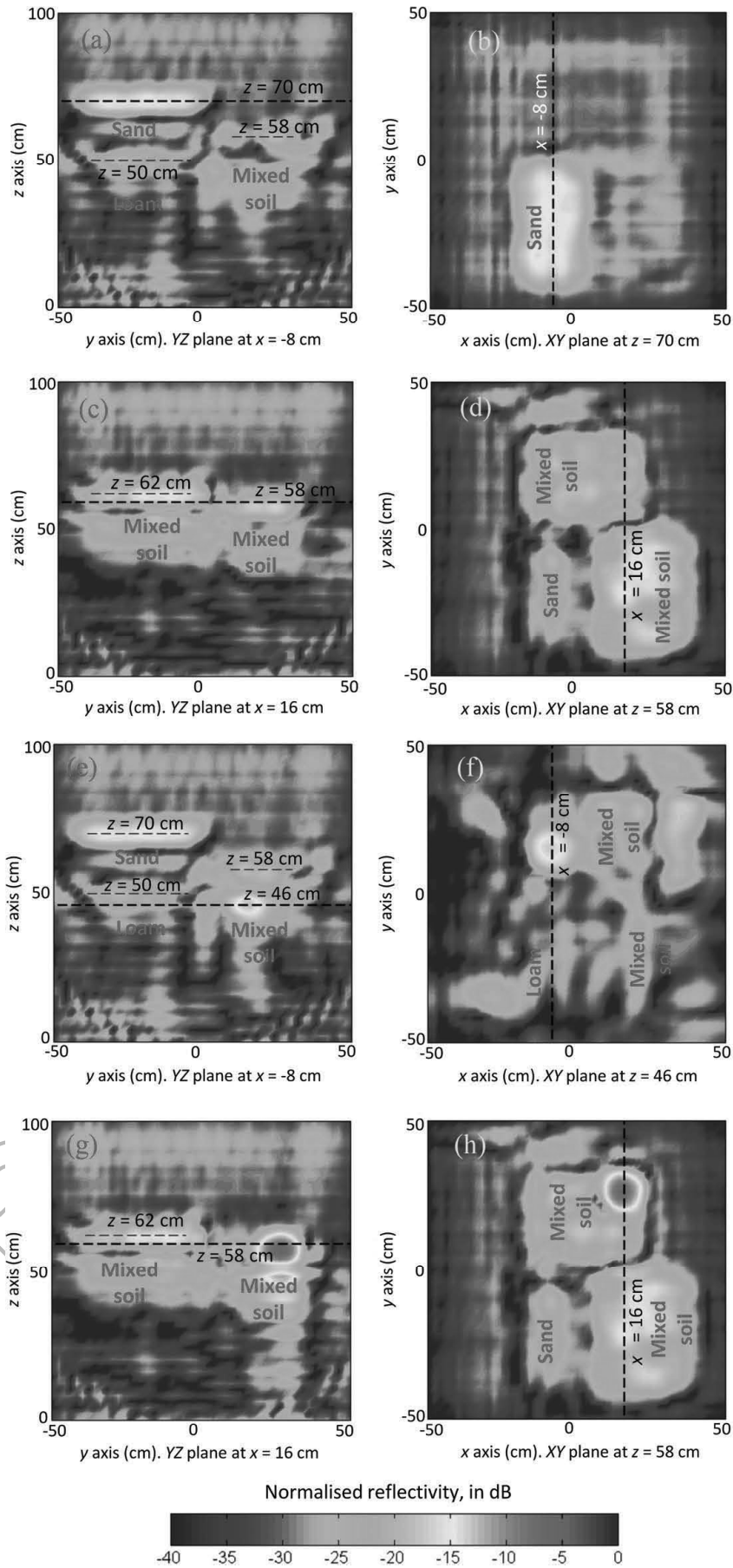


Figure 8. Measurement setup. (a) Right (small) box filled with 50% mix of sand and loam up to a height of 14 ± 1 cm. Left (large) box partially filled with 50% mix of sand and loam up to a height of 18 ± 1 cm, with the other half filled with a layer of loam and an upper layer of sand (detailed in (b)).

COLOUR
FIGURE



COLOUR
FIGURE

Figure 9. Reflectivity SAR images. XY, XZ, and YZ plane cuts. (a–d) Boxes with no metallic targets. (e–f) Metallic target buried 7 cm in the mixed soil. (g–h) Metallic target placed on top of the mixed soil box.

Table 1. Permittivity reconstruction results.

Soil	Figure	$\Re(\epsilon_{r,c})$	$\Im(\epsilon_{r,c})$	Reference values
Sand	Figure 3	[2.7 3.5]	[0.27 0.41]	$\Re(\epsilon_{r,c})=2.55$ (<i>Dielectric Constant</i> , 2016)
	Figure 7 (sand box)	[2.8 3.5]	N/A	$\Re(\epsilon_{r,c})= [2.7 3.7]$, $\Im(\epsilon_{r,c})=[0.05 0.5]$ (Wang and Schmutge 1980)
	Figure 7 (sand box)	[2.8 4.0]	N/A	
	Figure 11 ($d_{obj} = 20$ cm)	[2.9 3.2]	[0.32 0.47]	$\Re(\epsilon_{r,c})= [3 6]$, $\Im(\epsilon_{r,c})=[0.7 0.8]$ (Gadani and Vyas 2008, Figure 8(a))
	Figure 11 ($d_{obj} = 15$ cm)	[2.7 3.2]	[0.32 0.40]	$\Re(\epsilon_{r,c})= [2.5 2.55]$, $\Im(\epsilon_{r,c})=[0.02 0.03]$ (Abdelgwad and Said 2016) $\Re(\epsilon_{r,c})= 3.05$, $\Im(\epsilon_{r,c})=0.26$ (Komarov, Wang, and Tang 2005) $\Re(\epsilon_{r,c})= 2.6$ (dry sand) (Matzler 1998) $\Re(\epsilon_{r,c})= [3 4]$, $\Im(\epsilon_{r,c})=[0.1 0.4]$ (Vall-Llossera et al. 2005)
Loam	Figure 5	[2.5 3.2]	[0.58 0.88]	$\Re(\epsilon_{r,c})= [3 4]$, $\Im(\epsilon_{r,c})=[0.2 0.7]$ (Vall-Llossera et al. 2005)
Mixed soil	Figure 9	[2.4 3.4]	[0.38 0.58]	$\Re(\epsilon_{r,c})= [3 5]$, $\Im(\epsilon_{r,c})=[0.1 0.6]$ (Gadani and Vyas 2008, Figure 8(b))

Loss tangent ($\tan \delta$) defined as: $\tan \delta = \Im(\epsilon_{r,c}) / \Re(\epsilon_{r,c})$ (*Dielectric Constant*, 2016).

Soil moisture from 3% to 7% (Vall-Llossera et al. 2005).

of samples in laboratory, or indirect observation techniques, and the ones obtained with the proposed SAR-based technique. Note that the samples used in this contribution and in the literature may vary in the composition, thus resulting in different permittivity ranges as noticed in Table 1. This is especially noticeable in the case of $\Im(\epsilon_{r,c})$, which is more sensitive to soil moisture (Vall-Llossera et al. 2005). 260

4. Outdoor scenario

4.1. Soil characterization

The proposed methodology has been validated in a realistic outdoor scenario, a sandy beach (coordinates 43.547, -5.589). For this test, a PulsON P410 monostatic radar module (PulsOn Radar Module 2016) working from 3.1 to 5.3 GHz has been used. The radar module has been mounted on a platform that allows manual scanning in cross-range (x -axis), as depicted in Figure 10. The radar module is connected to a laptop for data collection and processing. Cross-range scanning is performed 45 cm above the surface of the beach creating a synthetic aperture of 1 m sampled every 2 cm (0.35λ at 5.3 GHz). The target is a circular metallic target of diameter 18 and 1 cm thickness. 270

First, the sand permittivity is characterized. For this purpose, the target is buried at a known depth of $d_{obj} = 20$ cm (see Figure 10). When conventional SAR imaging is applied, Figure 11(b), it can be observed that the echo of the metallic target appears 35 ± 1 cm below the soil surface, so $d_{echo} = 35 \pm 1$ cm $- d_{obj} = 15 \pm 1$ cm. By applying Equation (5), the estimated relative permittivity of the sand is $\Re(\epsilon_{r,c}) = [2.9 3.2]$. 275

In order to estimate the imaginary part of the permittivity, an additional measurement with the metallic target uncovered (as in Figure 10) is performed. The recovered reflectivity is depicted in Figure 11(a). As observed in Figure 11(b), the amplitude of the echo due to the reflection on the buried metallic target is $|\rho_{buried}(d_{obj})| = -14 \pm 1$ dB ($z = 82$ cm), and from Figure 11(a), when the target is on top of the sand, $|\rho_{top}(d_{obj})| = 0 \pm 1$ 280

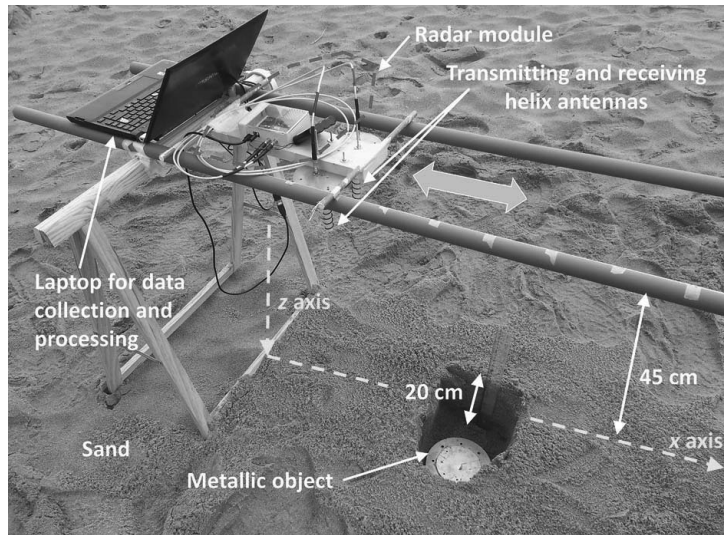
COLOUR
FIGURE

Figure 10. GPR measurement setup deployed in a realistic scenario (sandy beach) and placement of the metallic target.

dB. Then, $\alpha = [8.2 \ 9.0]$. Finally, after applying Equation (7), $\Im(\epsilon_{r,c}) = [0.32 \ 0.37]$ (centre frequency, 4.2 GHz).

285

The same experiment has been repeated with the object buried in another position at a depth of $d_{obj} = 15$ cm. Results are depicted in Figure 11(c). For this case, $\Re(\epsilon_{r,c}) = [2.7 \ 3.2]$ and $\Im(\epsilon_{r,c}) = [0.32 \ 0.40]$, in agreement with the previous case.

4.2. Application to Underground-SAR

Once the capability of the proposed conventional SAR-based technique to recover the permittivity of the medium has been proved, practical application of the interest on accurate permittivity estimation is shown in this section.

290

Conventional SAR imaging results depicted in Figure 11(b) and 11(c) show that the buried target is detected at a depth of 35 cm and 26 cm, that is, about 75% deeper than expected. For some GPR applications where just detection is required it is not a major drawback. However, in fields such as civil engineering or archaeology, accurate estimation of the depth is required in order to avoid damaging the buried object (metallic pipe, buried artwork, etc.).

295

The estimated permittivity of the sand (centre value of the estimated range, $\Re(\epsilon_{r,c}) = 3.0$ and $\Im(\epsilon_{r,c}) = 0.35$) has been introduced as an input in an Underground-SAR imaging algorithm (see Figure 1 flow chart). The recovered reflectivity is depicted in Figure 12. Note that the metallic target buried at $d_{obj} = 20$ cm is now imaged at a depth of 21 ± 1 cm (Figure 12(a)), and when buried at $d_{obj} = 15$ cm, the metallic object reflection is detected at 14 ± 1 cm (Figure 12(b)). In both cases, depth estimation error is less than 10%.

300

5. Conclusions

From the experimental results presented in this contribution, it can be concluded that the proposed method for *in situ* characterization of the soil permittivity provides an accurate estimation of this parameter. Using the estimated permittivity value the

305

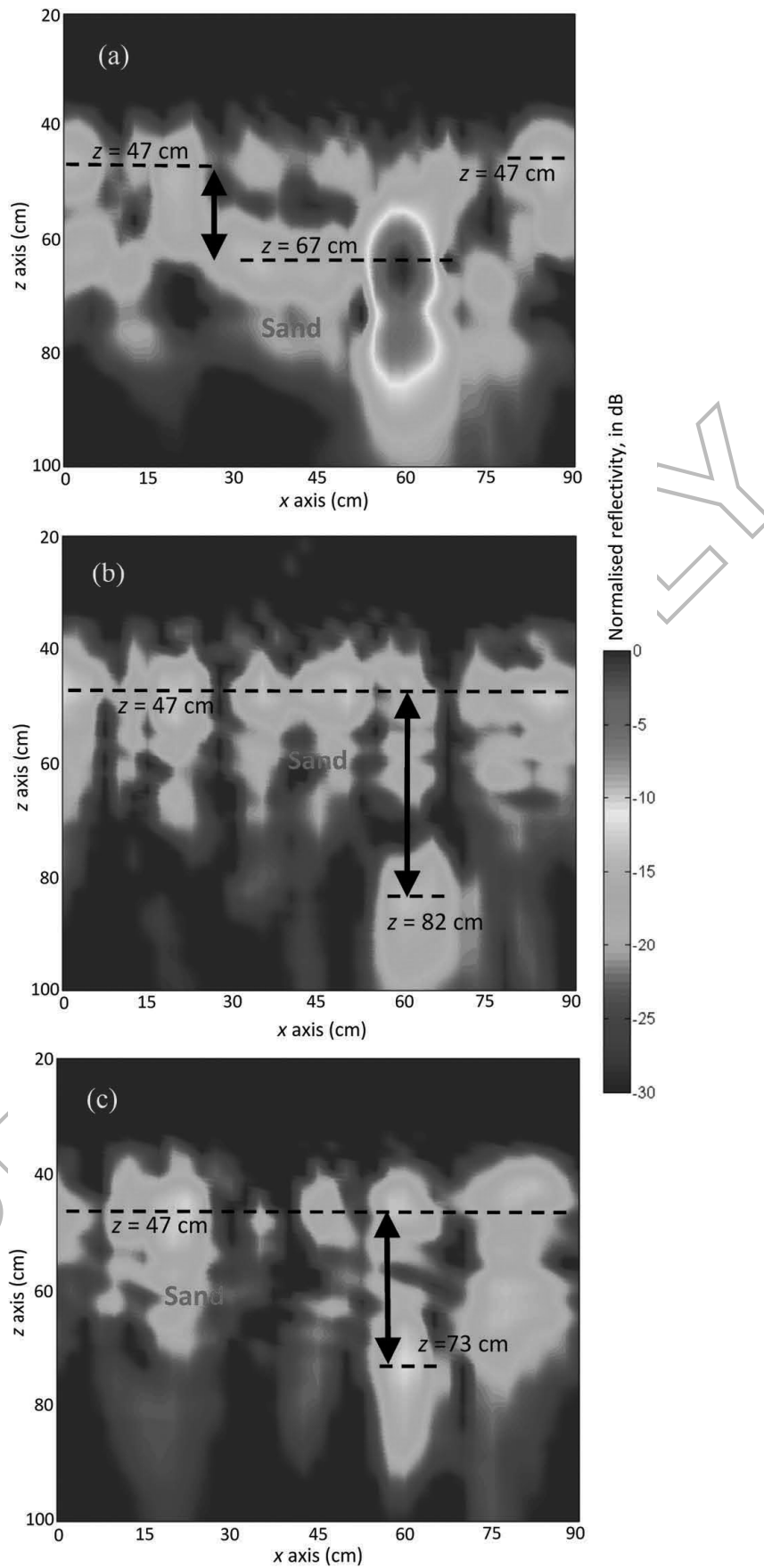


Figure 11. Reflectivity (amplitude, in dB, normalized with respect to the maximum of Figures 11 and 12) on XZ plane recovered from conventional SAR imaging. (a) Metallic target uncovered. (b) Metallic target buried at $d_{\text{obj}} = 20$ cm. (c) Metallic target buried at $d_{\text{obj}} = 15$ cm.

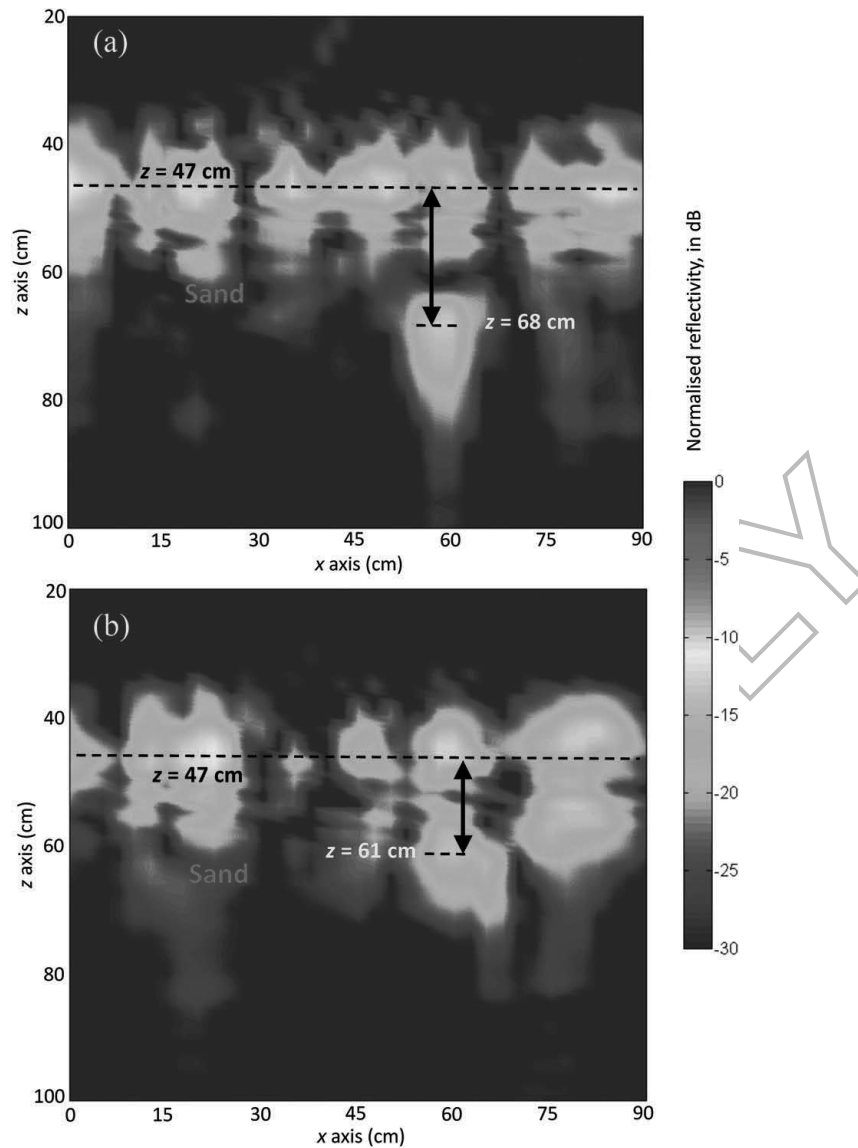
COLOUR
FIGURE

Figure 12. Reflectivity (amplitude, in dB, normalized with respect to the maximum of Figures 11 and 12) on XZ plane recovered from Underground-SAR imaging, with $\epsilon_{r,c} = 3.0 + j0.35$. (a) Metallic target buried at $d_{obj} = 20$ cm. (b) Metallic target buried at $d_{obj} = 15$ cm.

Underground-SAR imaging allows a correct recovery of the depth of buried targets, which can be of interest in applications such as civil engineering or archaeology.

One of the advantages of this method is that it avoids the need of additional hardware such as reflectometers, thus reducing the overall cost of the GPR system. Besides, it does not require additional measurements, since the information is extracted from the Underground-SAR images of the domain under test. The main drawback is that the method is invasive, as it requires burying a reference object in the soil to be characterized. However, once the permittivity is recovered, at the beginning and for a small part of the complete scenario, the same value is used for the whole reconstruction, assuming a homogeneous background medium.

An additional advantage of the proposed method is that, thanks to the fact that the depth and size of the reference target is known, it can be used to calibrate GPR parameters such as transmitting power or sensitivity from the resulting Underground-SAR image.

Acknowledgements

This work has been supported by the “Ministerio de Economía y Competitividad” of Spain/FEDER under project TEC2014-54005-P (MIRIEM), TEC2015-73908-JIN, MINECO-15-TEC2014-55290-JIN (PORTEMVISION), and grant FPU15/06341; by the Principado de Asturias, through the Plan de Ciencia, Tecnología e Innovación 2013-2017 under project GRUPIN14-114; and by the Galician Regional Government under Projects CN2012/279, CN2012/260 (AtlantTIC) and the Plan I2C (2011-2015). 325

Disclosure statement

AQ1 No potential conflict of interest was reported by the authors.

Funding

330

This work was supported by the Ministerio de Economía y Competitividad [FPU15/06341, MINECO-15-TEC2014-55290-JIN (PORTEMVISION), TEC2014-54005-P (MIRIEM), TEC2015-73908-JIN]; Gobierno del Principado de Asturias [GRUPIN14-114]; and Gobierno de Galicia [CN2012/260 (AtlantTIC), CN2012/279, Plan I2C (2011-2015)].

AQ3

Geolocation information

335

Outdoor measurements conducted at coordinates 43.547443, -5.589923.

ORCID

Yuri Álvarez López  <http://orcid.org/0000-0003-3625-4515>

References

- Dielectric Constant, Strength, and Loss Tangent. Accessed October 31, 2016. <http://www.rfcafe.com/references/electrical/dielectric-constants-strengths.htm> 340
- AQ4 Abdelgwad, A. H., and T. M. Said. 2016. “Measured Dielectric Permittivity of Contaminated Sandy Soil at Microwave Frequency.” *Journal of Microwaves, Optoelectronics and Electromagnetic Applications* 15 (2): 115–122. doi:10.1590/2179-10742016v15i2591.
- AQ5 Alvarez, Y., B. Gonzalez-Valdes, J. A. Martínez-Lorenzo, F. Las-Heras, and C. M. Rappaport. 2015. “SAR-Imaging-Based Techniques for Low-Permittivity Lossless Dielectric Body Characterization.” *IEEE Antennas and Propagation Magazine* 57 (2): 267–276. doi:10.1109/MAP.2015.2414492.
- Arbolea, A., Y. Alvarez, and F. Las-Heras 2013. “Millimeter and Submillimeter Planar Measurement Setup.” *Proceedings of 2013 IEEE Antennas and Propagation Society International Symposium (APSURSI)*: 1–2. Orlando (USA), 7-13 July. doi: 10.1109/APS.2013.6710661. 350
- Chen, C. C., J. T. Johnson, M. Sato, and A. G. Yarovoy. 2007. “Special Issue on Subsurface Sensing Using Ground-Penetrating Radar.” *IEEE Transactions on Geoscience and Remote Sensing* 45 (8): 2419–2421. doi:10.1109/TGRS.2007.902827.
- Daniels, D. J. 2006. “A Review of GPR for Landmine Detection.” *Sensing and Imaging: an International Journal* 7 (3): 90–123. doi:10.1007/s11220-006-0024-5. 355
- Gadani, D. H., and A. D. Vyas. 2008. “Measurement of Complex Dielectric Constant of Soils of Gujarat at X-And C-Band Microwave Frequencies.” *Indian Journal of Radio and Space Physics* 37: 221–229.

- Gamba, P., and V. Belotti. 2003. "Two Fast Buried Pipe Detection Schemes in Ground Penetrating Radar Images." *International Journal of Remote Sensing* 24 (12): 2467–2484. doi:10.1080/0143116021000050673. 360
- Gonzalez-Valdes, B., Y. Alvarez-Lopez, J. A. Martinez-Lorenzo, F. Las Heras Andres, and C. M. Rappaport. 2013. "SAR Processing for Profile Reconstruction and Characterization of Dielectric Objects on the Human Body Surface." *Progress in Electromagnetics Research* 138: 269–282. doi:10.2528/PIER13020607. 365
- Johansson, E. M., and J. E. Mast. 1994. "Three-Dimensional Ground-Penetrating Radar Imaging Using Synthetic Aperture Time-Domain Focusing." *Proceedings of SPIE – The International Society for Optical Engineering* 2275: 205–214. doi:10.1117/12.186717.
- AQ6 Komarov, V., S. Wang, and J. Tang. 2005. "Permittivity and Measurements." In *Encyclopedia of RF and Microwave Engineering*, 3693–3711. John Wiley and sons. doi:10.1002/0471654507.eme308. 370
- Liu, G., Y. Wang, J. Li, and M. R. Bradley. 2003. SAR Imaging for a Forward-Looking GPR System. *Proceedings of Aerosense 2003, International Society for Optics and Photonics* 5089: 322–333. Florida. 21-25 April. Doi:10.1117/12.485687.
- Marpaung, D. H. N., and Y. Lu 2014. "A Comparative Study of Migration Algorithms for UWB GPR Images in SISO-SAR and MIMO-Array Configurations." *Proceedings of 15th IEEE International Radar Symposium (IRS)*. Gdansk (Poland), 16-18 June. doi: 10.1109/IRS.2014.6869192. 375
- AQ7 Martinez, A., and A. P. Byrnes. 2001. *Modeling Dielectric-Constant Values of Geologic Materials: An Aid to Ground-Penetrating Radar Data Collection and Interpretation*. Kansas Geological Survey: University of Kansas.
- Martinez-Lorenzo, J. A., C. M. Rappaport, and F. Quivira. 2011. "Physical Limitations on Detecting Tunnels Using Underground-Focusing Spotlight Synthetic Aperture Radar." *IEEE Transactions on Geoscience and Remote Sensing* 49 (1): 65–70. doi:10.1109/TGRS.2010.2051952. 380
- Matzler, C. 1998. "Microwave Permittivity of Dry Sand." *IEEE Transactions on Geoscience and Remote Sensing* 36 (1): 317–319. doi:10.1109/36.65534.
- AQ8 PulsOn Radar Module. TimeDomain. Accessed 3 November 2016. <http://www.timedomain.com/p400-mrm.php> 385
- Robinson, D. A., S. B. Jones, J. M. Wraith, D. Or, and S. P. Friedman. 2003. "A Review of Advances in Dielectric and Electrical Conductivity Measurement in Soils Using Time Domain Reflectometry." *Vadose Zone Journal* 2 (4): 444–475. doi:10.2136/vzj2003.4440.
- Rosen, E. M., and E. Ayers. 2005. "Assessment of Down-Looking GPR Sensors for Landmine Detection." *Proceedings of SPIE - the International Society for Optical Engineering* 423–434. doi:10.1117/12.603831. 390
- Skierucha, W., A. Wilczek, A. Szyplowska, C. Sławiński, and K. Lamorski. 2012. "A TDR-Based Soil Moisture Monitoring System with Simultaneous Measurement of Soil Temperature and Electrical Conductivity." *Sensors* 12 (10): 13545–13566. doi:10.3390/s121013545. 395
- Sreenivas, K., L. Venkataratnam, and P. N. Rao. 1995. "Dielectric Properties of Salt-Affected Soils." *International Journal of Remote Sensing* 16 (4): 641–649. doi:10.1080/01431169508954431.
- Stove, G. C., J. McManus, M. J. Robinson, G. D. C. Stove, and A. Odell. 2013. "Ground Penetrating Abilities of a New Coherent Radio Wave and Microwave Imaging Spectrometer." *International Journal of Remote Sensing* 34 (1): 303–324. doi:10.1080/01431161.2012.713529. 400
- Vall-Llossera, M., M. Cardona, S. Blanch, A. Camps, A. Monerri, I. Corbella, F. Torres, and N. Duffo. 2005. L-Band Dielectric Properties of Different Soil Types Collected during the MOUSE 2004 Field Experiment. *Proceedings of the 2005 IEEE International Geoscience and Remote Sensing Symposium* 2: 1109. Seoul (South Korea). 25-29 July. Doi:10.1109/IGARSS.2005.1525309.
- Wang, J. R., and T. J. Schmugge. 1980. "An Empirical Model for the Complex Dielectric Permittivity of Soils as a Function of Water Content." *IEEE Transactions on Geoscience and Remote Sensing* 4: 288–295. doi:10.1109/TGRS.1980.350304. 405